ARL-TR-9505 ● AUG 2022

DEVCOM ARMY RESEARCH LABORATORY

Fracture Strength of SiC-Diamond Composite Microcantilevers

by Daniel Magagnosc

NOTICES

Disclaimers

The findings in this report are not to be construed as an official Department of the Army position unless so designated by other authorized documents.

Citation of manufacturer's or trade names does not constitute an official endorsement or approval of the use thereof.

Destroy this report when it is no longer needed. Do not return it to the originator.

ARL-TR-9505 ● AUG 2022

Fracture Strength of SiC-Diamond Composite Microcantilevers

Daniel Magagnosc
DEVCOM Army Research Laboratory

REPORT DOCUMENTATION PAGE

Form Approved
OMB No. 0704-0188

1. REPORT DATE *(DD-MM-YYYY)*	2. REPORT TYPE	3. DATES COVERED (From - To)
August 2022	Technical Report	1 June 2019–30 September 2021

4. TITLE AND SUBTITLE
Fracture Strength of SiC-Diamond Composite Microcantilevers

5a. CONTRACT NUMBER

5b. GRANT NUMBER

5c. PROGRAM ELEMENT NUMBER

6. AUTHOR(S)
Daniel Magagnosc

5d. PROJECT NUMBER

5e. TASK NUMBER

5f. WORK UNIT NUMBER

7. PERFORMING ORGANIZATION NAME(S) AND ADDRESS(ES)
DEVCOM Army Research Laboratory
ATTN: FCDD-RLW-MB
Aberdeen Proving Ground, MD 20115

8. PERFORMING ORGANIZATION REPORT NUMBER
ARL-TR-9505

9. SPONSORING/MONITORING AGENCY NAME(S) AND ADDRESS(ES)

10. SPONSOR/MONITOR'S ACRONYM(S)

11. SPONSOR/MONITOR'S REPORT NUMBER(S)

12. DISTRIBUTION/AVAILABILITY STATEMENT
Approved for public release: distribution unlimited.

13. SUPPLEMENTARY NOTES
ORCID ID: Daniel Magagnosc, 0000-0002-1418-9292

14. ABSTRACT
Silicon carbide (SiC)-diamond composites offer a combination of high hardness and fracture toughness with improved processability via reaction bonding. However, the inclusion of high diamond fractions creates new challenges in evaluating the mechanical properties by restricting sample machining methods. To circumvent some of these challenges, femtosecond laser micromachining is employed to fabricate microcantilevers. Using the microcantilevers, the fracture strength and fracture processes are examined. The mechanical testing results suggest that a strong bond is formed between the diamond particles and surrounding matrix. As a result, the fracture properties are comparable to monolithic diamond.

15. SUBJECT TERMS
silicon carbide, diamond, microcantilever, micromechanical testing, fracture, Sciences of Extreme Materials

16. SECURITY CLASSIFICATION OF:			17. LIMITATION OF ABSTRACT	18. NUMBER OF PAGES	19a. NAME OF RESPONSIBLE PERSON
a. REPORT	b. ABSTRACT	c. THIS PAGE			Daniel Magagnosc
Unclassified	Unclassified	Unclassified	UU	22	19b. TELEPHONE NUMBER (Include area code) (410) 278-4710

Standard Form 298 (Rev. 8/98)
Prescribed by ANSI Std. Z39.18

Contents

List of Figures iv

List of Tables iv

1. Introduction 1

2. Methods 1

3. Results 3

3.1 Diamond-SiC Composite Microstructure 3

3.2 Microcantilever Loading 4

3.3 Fractography and Flaw Strengths 6

4. Discussion 8

4.1 Strength Distributions 8

4.2 Deformation Process 9

5. Conclusion 10

6. References 12

List of Symbols, Abbreviations, and Acronyms 15

Distribution List 16

List of Figures

Fig. 1 Cantilever fabrication process 2

Fig. 2 a) BSE micrograph of the SiC-diamond composite microstructure and b) the segmented microstructure colored according to the phase 4

Fig. 3 Representative microcantilever viewed at 52° tilt 5

Fig. 4 Representative load-displacement response 5

Fig. 5 Example fracture initiation sites, indicated by white arrows, including a) distinct initiation within diamond particles and b) uncertain initiation site in SiC matrix 7

Fig. 6 Weibull distribution of fracture strengths in SiC-diamond microcantilevers. The marker indicates the phase and location of the fracture origin 9

Fig. 7 Cumulative distribution of critical stress intensity factor in SiC-diamond microcantilevers. The marker indicates the phase and location of the fracture origin. 9

List of Tables

Table 1 Summary of phase fraction and particle size statistics 4

Table 2 Microcantilever testing summary 6

Table 3 Summary of fracture initiation sites and estimated flaw toughness; *a* and *c* are the estimated fracture initiation site width and length, respectively 7

1. Introduction

Hard and ultrahard ceramics are of interest for applications that require high wear resistance. The combination of high hardness with good fracture toughness aids in minimizing the material removal rate during wear.[1,2] However, high-hardness ceramics are associated with significant processing limitations. For instance, fabrication of polycrystalline diamond, the current hardest known material with Vickers hardness on the order of 100 GPa, is generally limited to vapor deposited coatings or processing under high temperatures and pressures to produce a fully dense body.[3,4]

An alternative to monolithic, high-hardness ceramics is ceramic composites featuring a high-volume fraction of a high-hardness phase such as diamond. One such composite, silicon carbide (SiC)-diamond, may be produced via reaction bonding, which significantly lowers the temperature and pressure processing envelope.[5–8] The resulting materials offer hardness and fracture toughness similar or superior to that of SiC or boron carbide (B_4C)[9,10]; the hardness may even approach that of diamond.[11]

Given the excellent hardness of SiC-diamond composites, specimen fabrication for mechanical testing is a challenge. This challenge has restricted experimental analysis of the tensile and fracture properties. Multiple methods for cutting and polishing SiC-diamond have been examined and femtosecond laser (fs-laser) machining was identified as a viable method to mill the composites.[12] Here, fs-laser machining is employed to fabricate microcantilevers in mechanically polished SiC-diamond composites. The microcantilevers are then loaded to failure to assess the fracture strength under primarily tensile stresses.

2. Methods

Commercially produced reaction-bonded SiC-diamond composites were cut and polished from an initial 100- × 100- × 7-mm plate. The plate, consisting of 70%–80% diamond by volume, was laser cut to extract 8- × 8-mm sections; the sections were then thinned and polished to approximately 200-µm-thick using the scaif process by an external vendor.[12] The opposing faces of the section were polished parallel to each other. One such face was polished to an approximately 20-nm surface finish for fabrication of microcantilevers.

From the polished specimen microcantilevers were laser machined along one edge. Laser machining was performed using an fs-laser system consisting of a chirped pulse amplifier (CPA) fs-laser emitting at 775 nm with a repetition rate of 1 kHz.[13]

Typical laser pulse energies for machining the SiC-diamond composite were 10–20 μJ. The laser was focused using a 5× near infrared infinity corrected microscope objective resulting in a spot size of approximately 25 μm. Laser machining was then performed using a three-degree-of-freedom micropositioning stage to trace the desired shapes.

For laser machining, the sample was secured to a miniature goniometer stage. The goniometer stage was used to correct for the taper of the laser cut. Machining of the microcantilevers was accomplished via a multistep process. First, the length and width of the cantilever was established by cutting two trenches on the top polished surface parallel to the long axis of the cantilever. The specimen was then rotated 90° such that the laser impinged on the edge of the specimen. The thickness of the cantilever was then defined by cutting a trench parallel to the sample surface with sufficient depth and width to release the cantilever. Here, the specimen was pre-tilted using the miniature goniometer by about 10° to account for the taper in the laser cut. This ensured that the tension (top) and compression (bottom) surfaces of the microcantilevers were close to parallel—thereby simplifying the stress state. Finally, the end of the cantilever was released with a final cut at the prescribed length. The resulting cantilevers had a trapezoidal cross section. The fabrication process is illustrated in Fig. 1.

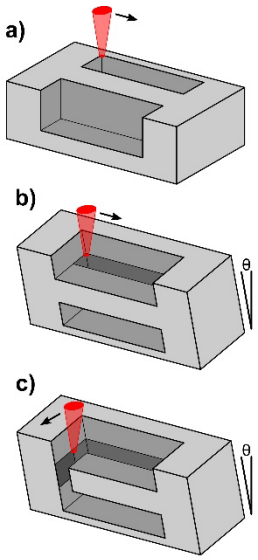

Fig. 1 Cantilever fabrication process

After fs-laser machining, each cantilever was examined in a scanning electron microscope (SEM) to measure the length, width, and height. Next, the sample was glued to an aluminum cylinder and mounted in a Keysight G200 nanoindenter. The nanoindenter was equipped with a 25 μm radius spherical diamond indenter. Using

the integrated optical microscope, the indenter tip was placed on the cantilever at a prescribed distance from the base of the cantilever. The cantilevers were loaded under load control at a nominal loading rate, $\dot{P}/P$ of 0.05 s^{-1}, until fracture. The load and displacement were recorded for each loading to be used in determination of the fracture strength.

After mechanical testing, each cantilever was again observed via SEM. These observations were used to measure the distance from the cantilever base at which fracture occurred. In addition, the fracture surface was observed to assess the fracture characteristics (i.e., initiation site and crack behavior).

Using the measured cantilever dimensions, the fracture strength was calculated from beam bending theory according to

$$\sigma_f = \frac{PL}{I} \tag{1}$$

where, P is the load at fracture, L is the distance from the fracture site to the loading point, and I is the moment of inertia. For the trapezoidal cantilever cross section employed here, I is calculated as

$$I = \frac{h^3(a^2+4ab+b^2)}{36(a+b)} \tag{2}$$

where, h is the cantilever thickness, a is the width at the top surface, and b is the width at the bottom surface.[14]

From the electron micrographs of the fracture surface, the fracture initiation site was identified and its dimensions were measured. Using this information, the critical stress intensity factor (K_C) was estimated for the strength limiting flaw for each cantilever according to

$$K_C = Y\sigma_f\sqrt{c} \tag{3}$$

where, Y is the stress intensity factor for a given flaw geometry and c is the critical flaw size. For each flaw, Y is determined according to the geometries described in Quinn.[15]

3. Results

3.1 Diamond-SiC Composite Microstructure

The as-prepared microstructure was observed via backscatter electron (BSE) imaging in the SEM (Fig. 2a). BSEs are sensitive to compositional differences and hence reveal the multiphase microstructure of the diamond-SiC composite. The microstructure consisted of a high-volume fraction of diamond particles (the dark

phase) surrounded by a continuous SiC matrix. Within the matrix an additional third unidentified phase is also observed. The phase fraction and particle size information were determined by segmenting the micrograph in ImageJ (Fig. 2b); the results are summarized in Table 1, where reported particle size statistics are weighted by particle area. The diamond particle sizes constituted a multimodal distribution; as a result the distribution was split at 30 μm and the average for the small and large particles is reported separately. No particle size is reported for the SiC as it forms a continuous network.

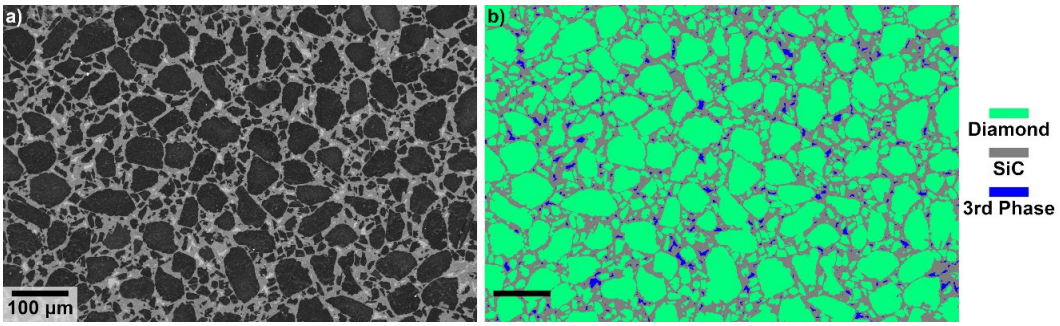

Fig. 2 a) BSE micrograph of the SiC-diamond composite microstructure and b) the segmented microstructure colored according to the phase

Table 1 Summary of phase fraction and particle size statistics

Phase	Phase fraction (%)	Particle size (μm)
Diamond	65.2	15.7 ± 5.3 / 71.1 ± 23.5
SiC	33.0	. . .
Third phase	1.8	7.3 ± 3.7

3.2 Microcantilever Loading

The fs-laser micromachined cantilevers were examined via SEM before mechanical testing to measure the critical dimensions. A representative microcantilever is included in Fig. 3. Here it is seen that the cantilever includes multiple diamond particles across the width and through the thickness. While this is typical, the number and size of diamond particles at the cantilever base varies as the cantilevers were randomly placed. In addition, some curtaining is observed along the cantilever side. This arises from dissimilar ablation rates between the diamond particles and the SiC matrix. However, the curtaining is not expected to significantly impact the stress calculations as it represents a small perturbation to the overall dimensions of the cantilever. In addition, the curtaining does not affect the top surface of the microcantilever where the maximum tensile stress occurs.

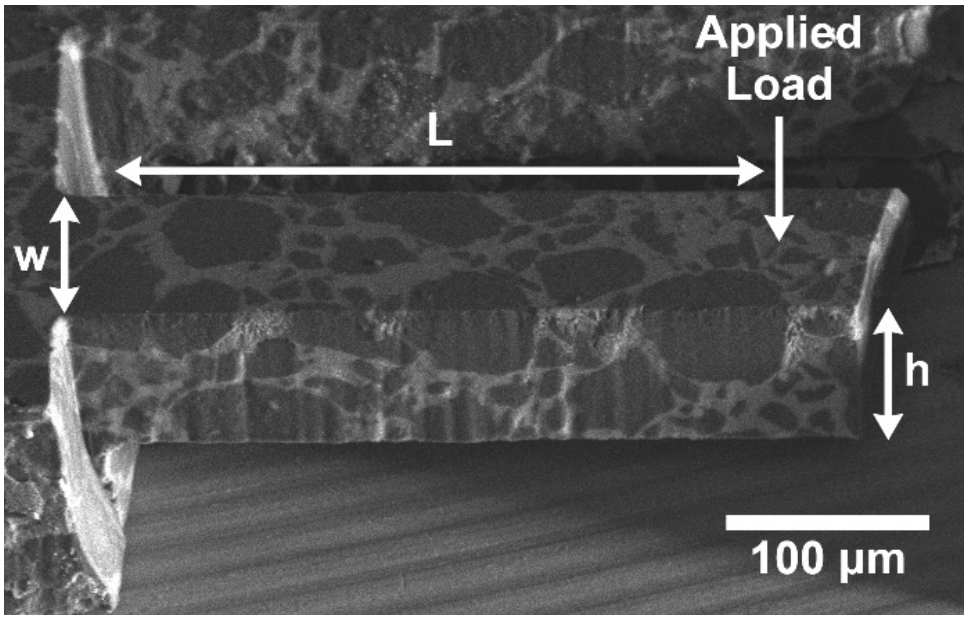

Fig. 3 Representative microcantilever viewed at 52° tilt

A representative load-displacement response of a microcantilever is shown in Fig. 4. The loading response consists of an initial transient as the diamond probe forms good contact with the surface. After the transient, linear elastic loading continues up to the maximum force at which point the cantilever fractures. Linear elastic loading was confirmed by repeated loading to forces less than the fracture load. The fracture stress was then calculated according to Eq. 1 and Eq. 2 using the dimensions measured from the SEM micrographs. The cantilever dimensions, maximum loads, and fracture stresses are summarized in Table 2.

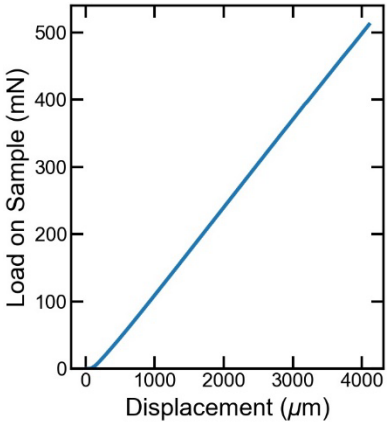

Fig. 4 Representative load-displacement response

Table 2 Microcantilever testing summary

Observation	*a* (μm)	*b* (μm)	*h* (μm)	*L* (μm)	P_{max} (mN)	Fracture stress (MPa)
1	97.0	123.3	80.3	315.8	0.577	1507
2	97.0	119.0	78.4	316.3	0.599	1709
3	93.7	120.7	79.6	319.6	0.458	1340
4	95.3	118.7	79.6	320.7	0.599	1708
5	93.7	118.3	79.9	322.3	0.504	1456
6	100.3	120.3	79.9	319.3	0.443	1201
7	97.3	120.3	80.6	321.6	0.325	909
8	95.7	120.7	80.9	326.1	0.395	1140
9	94.0	123.7	93.6	315.8	0.607	1140
10	98.3	124.0	92.0	322.0	0.601	1289
11	94.0	121.3	90.7	318.3	0.386	859
12	97.7	122.3	90.7	325.3	0.514	1160

3.3 Fractography and Flaw Strengths

Fracture surfaces were examined in the SEM to identify the fracture origin. Using a combination of BSE and secondary electron (SE) imaging, the fracture initiation site was identified and the phase and size were measured. Example fracture origins are presented in Fig. 5. The initiation sites were identified by tracing typical fractographic features (i.e., hackle). Generally, when fracture initiates within the diamond phase a distinct fracture origin is identified. In contrast, fracture origins in the SiC matrix tend to be more ambiguous. In all cases, well-defined fracture mirrors are not observed due to the small specimen size resulting in rapid fracture. In addition, the primary crack propagation path is found to be transgranular.

The fracture initiation sites are summarized in Table 3. From the summarized results, it is observed that the majority (eight observations) of fractures initiated within diamond particles; only one fracture was attributed to an origin at the SiC-diamond interface. The remainder (three observations) were identified as within the SiC matrix. Furthermore, the fracture locations were equally split between surface and near-surface origins. This indicates that the mechanical polishing process did not introduce surface defects.

In addition, the shape of each fracture origin was estimated as an ellipse. The major and minor axis of each origin was then measured; the resulting dimensions are summarized in Table 3 as *a* and *c*. Finally, the resulting critical stress intensity factor for each initiation site is calculated according to Eq. 3 using the stress

intensity factor for an elliptical flaw either at or near the surface. Here, the Newman–Raju formulas are used to determine Y.[15] The resulting critical stress intensity factors for each fracture origin are listed in Table 3.

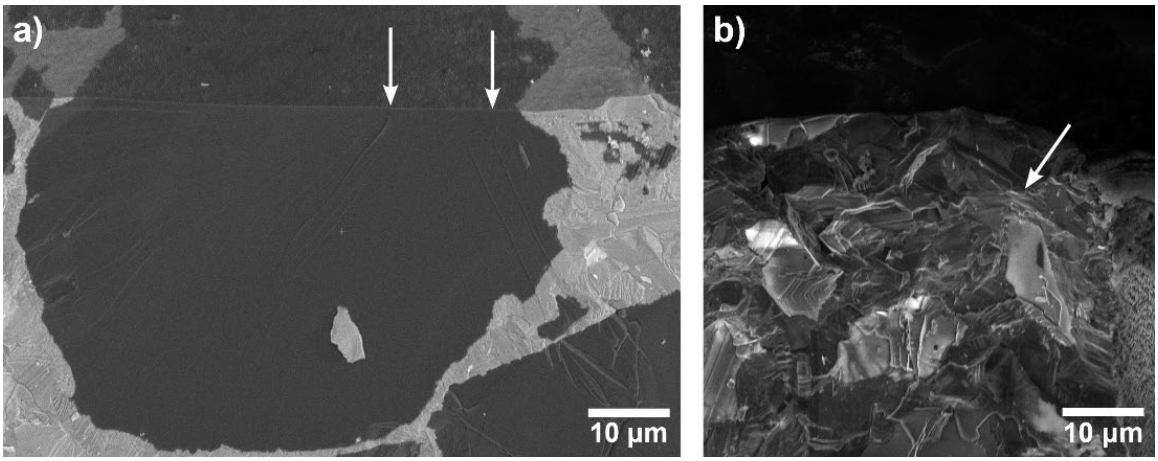

Fig. 5 Example fracture initiation sites, indicated by white arrows, including a) distinct initiation within diamond particles and b) uncertain initiation site in SiC matrix

Table 3 Summary of fracture initiation sites and estimated flaw toughness; *a* and *c* are the estimated fracture initiation site width and length, respectively

Observation	Fracture stress (MPa)	Location	a (µm)	c (µm)	K_C ($MPa\sqrt{m}$)
1	1507	Diamond, Near surface	2.67	4.99	4.68
2	1709	Diamond, Surface	2.33	4.54	4.29
3	1340	Diamond, Surface	0.81	2.61	2.32
4	1708	SiC, Near surface	0.77	4.10	6.22
5	1456	Diamond, Near surface	1.88	1.98	2.33
6	1201	Diamond, Near Surface	3.15	6.03	4.23
7	909	SiC, Surface	0.93	1.23	1.28
8	1140	Interface, Surface	0.39	2.07	1.47
9	1289	Diamond, Surface	1.59	8.55	3.42
10	1274	SiC, Near surface	0.88	2.79	3.68
11	859	Diamond, Surface	0.96	3.25	1.63
12	1160	Diamond, Near surface	1.93	2.54	2.45

4. Discussion

4.1 Strength Distributions

The distribution of fracture strengths in the SiC-diamond composite microcantilevers is examined in Fig. 6. After sorting the strength data, the probability was determined as $P = n - 0.5/N$, where n is the observation number and N is the total number of observations. Each marker is then labeled according to the phase (diamond, SiC, or interface) and location (surface or near surface) of the fracture origin. The resulting distribution is presented as a Weibull plot. A Weibull modulus ($\hat{m}$) and characteristic strength ($\hat{\sigma}_\theta$) of 5.61 and 1402 MPa, respectively, are determined according to a maximum likelihood estimation (MLE).

From the strength distribution, it is observed that the fracture origin (i.e., location and phase) does not show a systematic trend with strength. In other words, for the limited sample set studied here, the strength does not depend on the fracture origin. In addition, the strength distribution is well described by a Weibull distribution; the R^2 for the MLE fit is 0.9997. However, for the small sample size (N = 12) it is impractical to distinguish various probability distribution shapes (i.e., normal distribution vs. Weibull distribution).[16]

The calculated critical stress intensity factor for each cantilever is presented as a cumulative distribution in Fig. 7. Here the critical stress intensity for a given flaw appears to show a weak dependence on the fracture origin location. The surface flaws tend to exhibit a lower critical stress intensity factor. However, the phase of the fracture origin does not exhibit a trend with critical stress intensity factor. The resulting average critical stress intensity factor for flaws identified from the fracture surfaces is 3.17 ± 1.51 MPa·m$^{0.5}$.

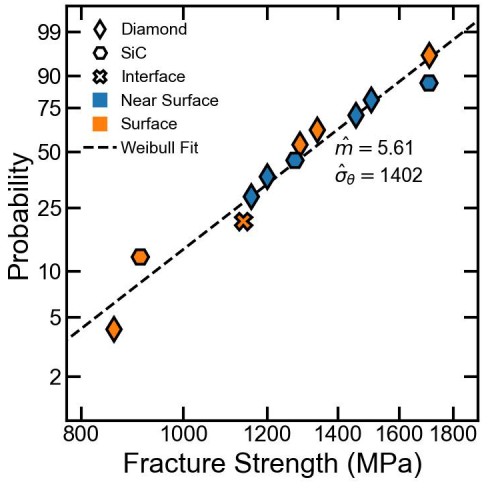

Fig. 6 Weibull distribution of fracture strengths in SiC-diamond microcantilevers. The marker indicates the phase and location of the fracture origin.

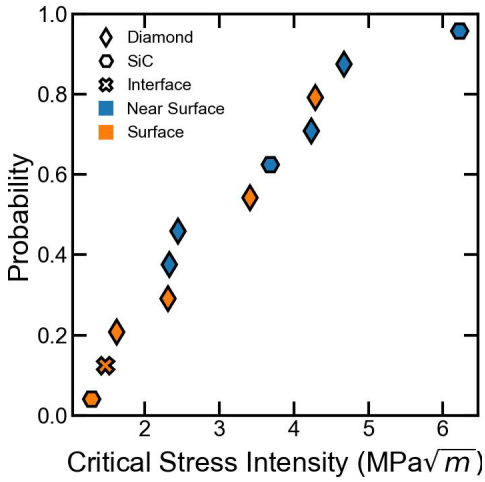

Fig. 7 Cumulative distribution of critical stress intensity factor in SiC-diamond microcantilevers. The marker indicates the phase and location of the fracture origin.

4.2 Deformation Process

Through examination of the fracture surfaces and the strength distributions a generalized fracture process for the diamond-SiC composite microcantilevers is proposed.

First, fracture tends to initiate within the diamond phase. This is indicated by prevalence of fracture origins within the diamond phase, regardless of the location (surface or near surface). While SiC possesses a lower average strength as compared to diamond, the smaller domain size of the SiC results in enhanced strength and toughness through the Hall–Petch effect.[17,18] Conversely, the large

diamond particles are expected to exhibit lower strength.[19–21] Hence, the much larger and more prevalent diamond particles are more likely to initiate the fracture process. In some instances, fracture clearly initiates at a well-defined flaw within a diamond particle. Such flaws are likely an inclusion, such as a metal-rich region, incorporated during the diamond production process.[22]

However, the apparent fracture toughness, as measured from the crack initiating flaw sizes, is lower than literature values for both polycrystalline and single crystal diamond. For instance, a polycrystalline chemical vapor deposition (CVD) diamond typically exhibits K_c of 5–10 MPa·m$^{0.5}$ depending on grade.[23,24] Given the comparable sizes of the large diamond particles and the cantilever dimensions a comparison to single crystal toughness is more apt. Yet even single crystal values (4–6 MPa·m$^{0.5}$) tend to be greater than the observed stress intensity factors for critical flaws.[25] The apparently low toughness observed in the microcantilevers likely stems in part from the uncertainty in measuring flaw sizes and from the small specimen geometries. For small specimens, the fracture initiating flaw is more prone to interacting with the free surface and crack propagation does not reach steady state.[26] Regardless, consideration of the apparent toughness relative to polycrystalline and single crystal diamonds suggest that modifying the toughness of the diamond phase may be an avenue to improve the mechanical response of SiC-diamond composites.

Once fracture initiates, the crack propagates along a tortuous path. Significant crack deflections are observed on all fracture surfaces. However, it is notable that the fracture surface transects the large diamond particles. Transgranular fracture indicates a strong interface between the diamond particles and the SiC matrix[27]; a weak interface would preferentially fracture before the diamond particles leading to intergranular fracture. This is supported by direct measurements of the SiC-diamond interface strength in similar composites.[28]

5. Conclusion

The mechanical response of SiC-diamond composites was investigated using microcantilever bending. Using fs-laser micromachining, microcantilevers were fabricated on the edge of a commercially sourced, mechanically polished coupon. After machining, the fracture strength was measured by loading the cantilevers in a nanoindenter.

By examining the fracture surfaces, the strength limiting flaw for each cantilever was identified. Consideration of the flaws revealed that fracture strength did not depend on the flaw type; failure primarily initiated within the large diamond particles. In addition, the critical stress intensity factor for each flaw was estimated.

Consideration of the apparent toughness relative to diamond suggests avenues for improving the mechanical properties. Finally, examination of the fracture surface revealed primarily transgranular fracture, which indicates a high SiC-diamond interfacial strength.

6. References

1. Hsu SM, Shen M. Wear prediction of ceramics. Wear. 2004;256(9–10):867–878.

2. Wang Y, Hsu SM. Wear and wear transition mechanisms of ceramics. Wear. 1996;195(1–2):112-122.

3. Hess P. The mechanical properties of various chemical vapor deposition diamond structures compared to the ideal single crystal. J Appl Phys. 2012;111(5):051101.

4. Haines J, Léger JM, Bocquillon G. Synthesis and design of superhard materials. Ann Rev Mater Res. 2001;31(1):1–23.

5. Herrmann M, Matthey B, Höhn S, Kinski I, Rafaja D, Michaelis A. Diamond-ceramics composites—new materials for a wide range of challenging applications. J Euro Ceram Soc. 2012;32(9):1915–1923.

6. Yang Z, He X, Wu M, Zhang L, Ma A, Liu R, Hu H, Zhang Y, Qu X. Fabrication of diamond/SiC composites by Si-vapor vacuum reactive infiltration. Ceram Int. 2013;39(3):3399–3403.

7. Matthey B, Höhn S, Wolfrum A-K, Mühle U, Motylenko M, Rafaja D, Michaelis A, Herrmann M. Microstructural investigation of diamond-SiC composites produced by pressureless silicon infiltration. J Euro Ceram Soc. 2017;37(5):1917–1928.

8. Mlungwane K, Herrmann M, Sigalas I. The low-pressure infiltration of diamond by silicon to form diamond–silicon carbide composites. J Euro Ceram Soc. 2008;28(1):321–326.

9. Zhao Y, Qian J, Daemen LL, Pantea C, Zhang J. Enhancement of fracture toughness in nanostructured diamond–SiC composites. Appl Phys Lett. 2004;84(8):1356–1358.

10. Vargas-Gonzalez L, Speyer RF, Campbell J. Flexural strength, fracture toughness, and hardness of silicon carbide and boron carbide armor ceramics. Int J Appl Ceram Tech. 2010;7(5):643–651.

11. Grodzinski P. Indentation hardness of diamond. Nature. 1956;177(4522):1228–1228.

12. Ligda JP, Shoulders T, DiGiovanni A. Sample preparation methods for diamond–silicon-carbide microstructure analysis. CCDC Army Research Laboratory (US); 2020. Report No.: ARL-TR-8887.

13. Magagnosc DJ, Ligda JP, Sano T, Schuster BE. Femtosecond laser machining of micro-tensile specimens for high throughput mechanical testing. In: Starman L, Hay J, editors. Springer International Publishing; 2018. p. 7–9 (Micro and Nanomechanics; vol. 5).

14. Gere JMTSP. Mechanics of materials. PWS Publishing Company; 1990.

15. Quinn GD. Fractography of ceramics and glasses. Natl Inst Stand Technol. 2016:7–17—7–29.

16. Danzer LC, Fischer FD. Fracture statistics of brittle materials: Weibull or normal distribution. Phys Rev E Stat Nonlin Soft Matter Phys. 2002;65(6 Pt 2):067102.

17. Rice RW. Ceramic tensile strength—grain size relations: grain sizes, slopes, and branch intersections. J Mater Sci. 1997;32(7):1673–1692.

18. Rice RW, Wu CC, Boichelt F. Hardness-grain-size relations in ceramics. J Am Ceram Soc. 1994;77(10):2539–2553.

19. Davies AR, Field JE, Pickles CSJ. Strength of free-standing chemically vapour-deposited diamond measured by a range of techniques. Philosoph Mag. 2003;83(36):4059–4070.

20. Davies AR, Field JE. The strength of free-standing CVD diamond. Wear. 2004;256(1–2):153–158.

21. Pickles CSJ. The fracture stress of chemical vapour deposited diamond. Diamond Relat Mater. 2002;11(12):1913–1922.

22. Yin L-W, Zou Z-D, Li M-S, Liu Y-X, Cui J-J, Hao Z-Y. Characteristics of some inclusions contained in synthetic diamond single crystals. Mater Sci Eng A. 2000;293(1–2):107–111.

23. Davies AR, Field JE, Takahashi K, Hada K. The toughness of free-standing CVD diamond. J Mater Sci. 2004;39(5):1571–1574.

24. Drory MD, Dauskardt RH, Kant A, Ritchie RO. Fracture of synthetic diamond. J Appl Phys. 1995;78(5):3083–3088.

25. Liang Q, Yan C-S, Meng Y, Lai J, Krasnicki S, Mao H-K, Hemley RJ. Enhancing the mechanical properties of single-crystal CVD diamond. J Phys Condens Matter. 2009;21(36):364215.

26. Magagnosc DJ, Schuster BE. Fracture strength of hot-pressed silicon carbide at the microscale. Mater Sci Eng A. 2019;765:138297.

27. Wolfrum A-K, Quitzke C, Matthey B, Herrmann M, Michaelis A. Wear behavior of diamond-silicon nitride composites sintered with FAST/SPS. Wear. 2018;396–397:172–181.

28. Ast J, Matthey B, Herre P, Höhn S, Herrmann M, Christiansen SH. Micro-cantilever testing of diamond-silicon carbide interfaces in silicon carbide bonded diamond materials produced by reactive silicon infiltration. Open Ceram. 2021;8:100176.

List of Symbols, Abbreviations, and Acronyms

ARL	Army Research Laboratory
B_4C	boron carbide
BSE	backscatter electron
CPA	chirped pulse amplifier
CVD	chemical vapor deposition
DEVCOM	US Army Combat Capabilities Development Command
fs-laser	femtosecond laser
MLE	maximum likelihood estimation
SE	secondary electron
SEM	scanning electron microscope
SiC	silicon carbide

1 (PDF)	DEFENSE TECHNICAL INFORMATION CTR DTIC OCA
1 (PDF)	DEVCOM ARL FCDD RLD DCI TECH LIB
12 (PDF)	DEVCOM ARL FCDD RLD FS S COLEMAN FCDD RLW B J LASALVIA FCDD RLW MB J LIGDA B LOVE D MAGAGNOSC B POWERS FCDD RLW ME A DIGIOVANNI M GUZIEWSKI L VARGAS-GONZALEZ FCDD RLW TE T SCHARF FCDD RWL TB J CLAYTON FCDD RWL TF D MALLICK